Electron energy-loss study of the electronic structure of atomic scale $SrTiO_3$-$SrMnO_3$-$LaMnO_3$ superlattices

Amish B. Shah,[1,2] Xiaofang Zhai,[2,3] Bin Jiang,[1,2] Jian-Guo Wen,[2] James N. Eckstein,[2,3] and Jian-Min Zuo[1,2]
[1]*Department of Materials Science and Engineering, University of Illinois at Urbana-Champaign, Urbana, Illinois 61801, USA*
[2]*F. Seitz Materials Research Laboratory, University of Illinois at Urbana-Champaign, Urbana, Illinois 61801, USA*
[3]*Department of Physics, University of Illinois at Urbana-Champaign, Urbana, Illinois 61801, USA*
(Received 13 September 2007; revised manuscript received 18 December 2007; published 4 March 2008)

$SrTiO_3$ (STO), $SrMnO_3$ (SMO), and $LaMnO_3$ (LMO) ultrathin films with layer thicknesses of 1–4 perovskite unit cells were grown on a STO substrate. The physical and electronic structures of ultrathin films and interfaces were characterized with nanoarea electron diffraction, scanning transmission electron microscopy (STEM), and electron energy-loss spectroscopy (EELS). The diffraction patterns show that the epitaxial growth of LMO, SMO, and STO with strain is closely lattice matched to the STO substrate. High resolution *Z*-contrast STEM images clearly show the superlattice structure with atomically sharp interfaces. EELS shows changes in the density of unoccupied states of oxygen, which is present in all films, and of titanium at the STO-SMO interface. We find that the O *K* edge in layered LMO shifts depending on the thickness of the film. No peak shifts of Mn in $LaMnO_3$ and $SrMnO_3$ are observed within our instrument resolution, indicating that the valence of the Mn ion is approximately constant across the interface while the electron density of oxygen atoms accepts the local charge transfer.

DOI: 10.1103/PhysRevB.77.115103 PACS number(s): 79.20.−m, 73.21.Cd, 73.21.Ac

INTRODUCTION

Perovskites grown on $SrTiO_3$ (STO) have attracted considerable interest recently since the corner-linked octahedral network structure of perovskites can accommodate a large amount of lattice strain during epitaxial growth. Bulk transition metal perovskites exhibit a range of important physical properties from insulating to conducting transport, including high temperature superconductivity, ferromagnetism, and ferroelectricity.[1–3] Past studies have shown that large changes in properties of transition metal oxides can be induced with small changes in hole on electron concentration and external factor such as electric and magnetic fields.[4–6] By combining different perovskites in an epitaxial superlattice, it is expected that alternating lattice matched perovskite superlattices can result in unexpected electronic properties. For example, Okamoto and Millis found that in a film consisting of $SrTiO_3$ and $LaTiO_3$ layers, leakage of charge at an interface of two insulators can lead to reconstruction and metallic behavior.[7] In a superlattice, the electronic properties will depend on the thickness of the layers. In $SrTiO_3$-$LaTiO_3$ superlattices, the center Ti ion does not exhibit bulk electronic properties when the number of $LaTiO_3$ unit cells is less than 5.[8]

In this paper, we report a study of $LaMnO_3$ (LMO), $SrMnO_3$ (SMO), and STO interfaces by a combination of synthesis and characterization. The reported lattice constants for bulk STO, LMO, and SMO are 3.91, 3.95, and 3.81 Å respectively.[8,9] Epitaxial, lattice matched films of LMO, SMO, and STO can be formed without misfit dislocations from one layer to the next.[10] We have grown a complex superlattice with multiple layers of thickness 1–4 atomic layers each, using atomic layer-by-layer molecular beam epitaxy. Nanoarea electron diffraction (NED), scanning transmission electron microscopy (STEM), and electron energy-loss spectroscopy (EELS) were used to investigate the interfaces. NED shows superlattice reflections from a small region and allows us to determine epitaxial strain and the average repeat distance of the superlattice. Core loss EELS is used to reveal information about ionization of cations, especially O and Mn ions, and provides a fingerprint of electronic structure at the interfaces. The LMO-SMO layers are grown with insulating STO films on both sides. This special architecture allows us to study the Mn states in these superlattices as a function of film thickness, which are critical to the electronic and magnetic properties of manganite films.[10–13]

EXPERIMENT

Films of STO, SMO, $SrTi_{0.9}Mn_{0.1}O_3$ (STMO), and LMO were grown as a multilayer superlattice on a ⟨100⟩ $SrTiO_3$ substrate. The superlattice is shown in Fig. 1. The films are deposited by molecular beam epitaxy (MBE). Prior to growth, the (100) $SrTiO_3$ substrate was cleaned in 10:1 diluted HCl. The MBE base pressure is 5×10^{-9} Torr. The deposition is performed in a pure ozone environment with 2×10^{-6} Torr pressure. The elemental sources are effusion cells. The atomic beam fluxes are measured by atomic absorption spectroscopy or using a quartz crystal microbalancer, depending on element. The absolute accuracy was calibrated by Rutherford backscattering spectroscopy. The films are grown a single atomic layer at a time at a temperature of 700 °C. Reflection high energy electron diffraction is used to monitor the growth. After each atomic layer is grown, the shutters to the effusion cells are closed and the sample is annealed for 1 min.

Samples for electron microscopy were prepared by mechanical wedge polishing. The sample was glued to a clean glass slide and wedge polished with a 1° angle. The sample was ion milled with Gatan Precision Ion Polishing for several hours at 4.0 kV, and fine polished for 20 min at 2.0 kV. The sample was cleaned in a Fischione plasma cleaner and

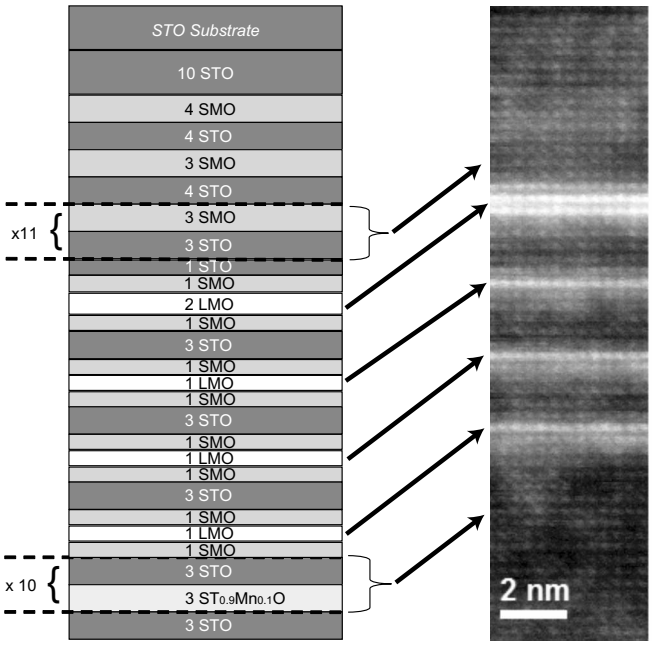

FIG. 1. The superlattice recipe for growth and high resolution *Z*-contrast image of the superlattice. All films in the recipe are shown as number of unit cells and are not drawn to scale. The areas marked with dashed lines are repeated supercells. Growth steps are observed in other parts of the sample but are not shown here.

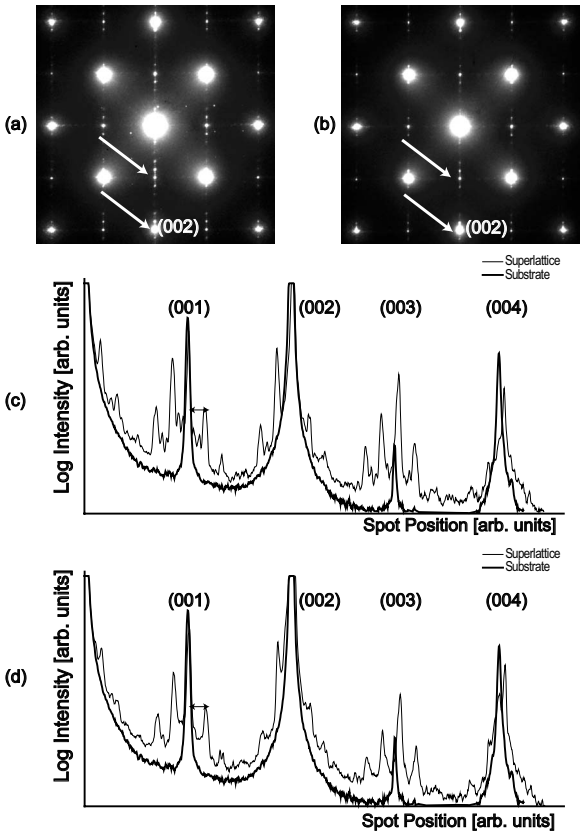

FIG. 2. (a) Nanobeam diffraction pattern of the LMO-SMO-STO region and (b) SMO-STO region. [(c) and (d)] Line profiles of the reflections marked by the arrows in (a) and (b), respectively. For comparison, the line profile of the STO substrate, which is used for calibration, is also plotted here.

then directly transferred to the microscope. NED, STEM, and EELS were performed on a JEOL 2010F transmission electron microscope (TEM) operating with an acceleration voltage of 200 kV and C_S of 1.0 mm. STEM images were acquired with a transmitted electron imaging (TEI) annular dark-field detector, and EELS spectra were acquired with a Gatan Image Filter model 2001. The EELS dispersion was selected at 0.49 eV/channel.

NED patterns was obtained with a probe size of 40 nm. STEM/EELS data was collected with a probe size of <1 nm and a half convergence angle of 7.5 mrads. EELS line scans were 7–25 nm in length and the integration time was 7–8 s per point. Core loss energy peaks were recorded between ~400 and 900 eV. Ti $L_{2,3}$, O K, Mn $L_{2,3}$, and $La_{4,5}$ peaks are visible in the EELS spectra. Background subtraction was performed with a power law at each of these peaks. The Ti L_1 peak is visible in some spectra, but since its energy-loss value is too close to the O K edge, background subtraction is noisy and unreliable. Therefore, discussion of Ti is limited to the $L_{2,3}$ edge.

RESULTS AND DISCUSSION

Figure 1 shows a recipe for growth and a high resolution *Z*-contrast STEM image of the superlattice. The superlattice is 177 unit cells in thickness (~70 nm) and comprised of STO, SMO, LMO, and $ST_{0.9}M_{0.10}O$ thin films. The STEM image was recorded using a selected probe size of 0.2 nm optimized for STEM image resolution. The bright white lines are the LMO films. Growth steps were observed in other parts of the sample, but are not displayed here. Figure 2 shows NED diffraction patterns taken with a probe size of 40 nm of the LMO-SMO-STO region and SMO-STO region. In the first diffraction pattern, the probe covers the LMO-SMO-STO region and some of the underlying SMO-STO film growth. Sharp superlattice reflections are observed in the diffraction pattern. Comparing the position of the superlattice reflections from the line profile through the strong {001} spots to the substrate reflections reveals an averaged lattice repeat distance of 6.3 ± 0.2. The repeat comes from three of the four repeat cells, which were grown as six unit cells and one of the films is grown as seven unit cells. Similar superlattice reflections are observed in a diffraction pattern recorded at the SMO-STO region, which is closer to the substrate. The repeat distance measured from this diffraction pattern is 6.4 ± 0.1. The STO/SMO repeat distance is grown as six unit cells for the majority of films. In both cases, the measured superlattice repeat is close to the experimental growth parameter. Line profiles through the diffraction pattern are shown to display higher order reflections. The comparison of the diffraction profile with that of the STO substrate shows that the SMO/STO superlattice is contracted normal to the substrate; the contraction is measured as 1.6% and $1.0\% \pm 0.2\%$ using the (003) and (004) peaks, respectively. Contraction is expected as bulk SMO has a smaller lattice parameter than the STO substrate. The LMO-SMO-STO films are less contracted compared to STO/SMO; the

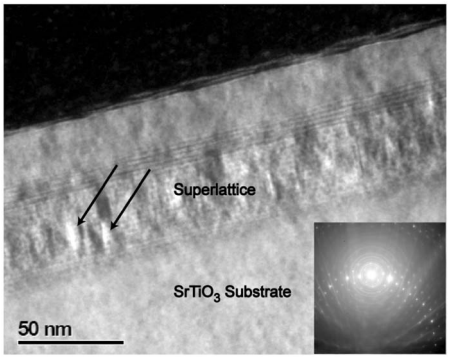

FIG. 3. A dark-field TEM image of the superlattice showing strong diffraction contrast in the SMO-STO region. The inset is a diffraction pattern showing the diffraction condition used for imaging the 020 reflection, with the 004 near the Bragg diffraction condition.

measured contractions with respect to the substrate are 1.0% and 0.9% ± 0.2% using the (003) and (004) peaks, respectively. Bulk LMO has a larger lattice parameter than bulk STO; however, the difference is not as large as that between STO and SMO. The contraction is observed here with five layers of LMO being grown compared to eight layers for SMO. The measurement of lattice parameter using the (004) reflection is somewhat problematic; the (004) peak observed consists of multiple peaks. The dominant peak is used to calculate the lattice parameter. In comparison, the (003) usually has only a single peak, which gives more consistent results. Figure 3 shows a dark-field image recorded using the 020 beam perpendicular to the interface. No misfit dislocation was observed at the superlattice/substrate interface. Interestingly, strong diffraction contrast is observed in the superlattice, which indicates local changes in diffraction condition due to strain. The change can come from strain relaxation during cross sectioning and ion milling, or from growth. A comparison with small angle, high resolution, x-ray diffraction is needed to distinguish between these two mechanisms.

Figure 4(a) shows a STEM image and EELS spectrum images of the superlattice through the LMO-SMO-STO region. The probe size selected at 0.3 nm in this case was optimized to improve the counting statistics for EELS. To determine the actual probe size at the specimen, the intensity was integrated from the background subtracted Ti $L_{2,3}$, Mn $L_{2,3}$, and La $M_{4,5}$ peaks. These integrated intensities and line profile of the Z-contrast image are shown in Fig. 3(b). The length axis for the Z-contrast image is scaled to the number of points in the EELS line scan. The second, third, and fourth peaks in the La $M_{4,5}$ spectrum correspond to single unit cell layers of LMO grown, and are the basis for determining the probe size. There are five unit cells of STO/SMO in between the single layer LMO films with a thickness of ~20 Å and length of 7 pixels in the line scan. The probe size during EELS acquisition was estimated using the STEM intensity profile of the single La layer, which can be fitted by a Lorentzian function with a full width at half maximum (FWHM) of 5.7 ± 0.8 Å. The EELS spatial resolution is, thus, limited mostly by the probe size in this case. The

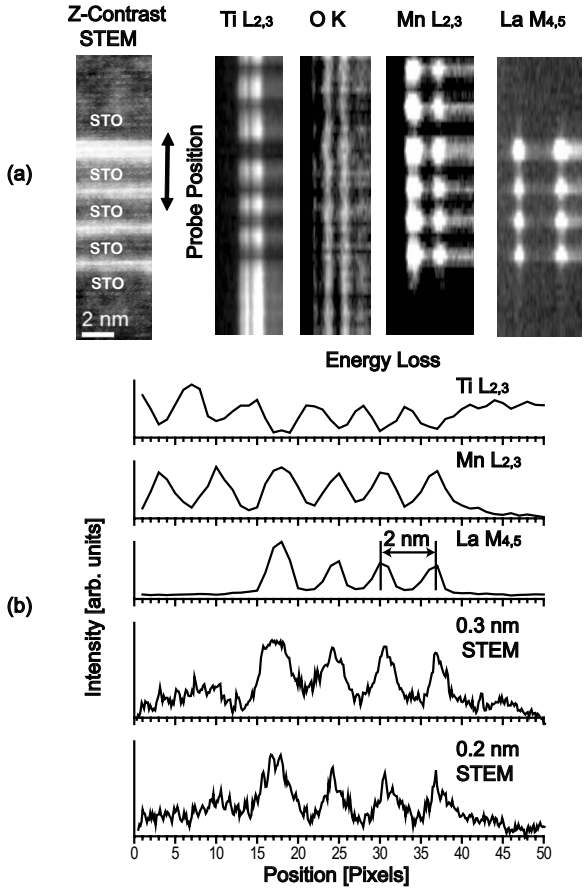

FIG. 4. (a) A Z-contrast image of the superlattice through the LMO-SMO-STO films. The inserted EELS spectra are the Ti $L_{2,3}$, O K, Mn $L_{2,3}$, and La $M_{4,5}$. The O K prepeak is visible in the STO layers. The O K edge shifts in the different perovskite films. (b) Summed intensity from the background subtracted Ti $L_{2,3}$, Mn $L_{2,3}$, and La $M_{4,5}$ peaks, and intensity profile of the Z contrast. For comparison, the intensity profile of the higher resolution Z-contrast STEM image in Fig. 1 is provided. The intensity profile of the single LO layer can be fitted using the Lorentzian function, which is 5.7 ± 0.8 Å in FWHM. The probe measured here is for EELS acquisition; a smaller probe is available for high resolution STEM imaging.

Lorentzian function has a large tail; experimentally, this shows up as increased intensity in SMO and STO between LMO layers. The LMO peak to background ratio is 1.5 for single layered LMO and 1.6 for double layered LMO. For comparison, a line profile of the higher resolution STEM image in Fig. 1 is shown, where a smaller probe size of 0.2 nm was selected in the software controls for higher spatial resolution. The region of sample is slightly different from the previous case; therefore, the smallest feature sizes in each image are used for comparison. The width of the LMO peak in this high resolution image is 3 Å, and the peak to background ratio is 1.8 for single layered LMO and 2.1 for double layered LMO. The tail at 9 Å is slightly narrower than the previous case. The spatial resolution is improved, and the contrast is higher.

At the top of Fig. 4(a) is the SMO/STO films and at the bottom is a STO-STMO region where Mn doping is esti-

mated at 10%. The middle region with white lines is the LMO/SMO/STO films. The corresponding EELS spectra of the middle region are shown in Fig. 5(a). Only part of the line scan is shown here, indicated by the arrow in Fig. 4(a). Three O *K* peaks are visible. According to Verbeeck *et al.*[14,15] and Abbate *et al.*,[16] these are excitations of the O 1*s* core states to O 2*p* states hybridized with Mn 3*d*, La 5*d* or Sr 4*d*, and Mn 4*sp*. The first peak, which is referred to as the prepeak, is attributed to transitions between the O 1*s* core state to the 2*p* state, which is hybridized with Mn 3*d* orbitals.[2,17,18] de Groot *et al.* have shown that the prepeak may consist of several peaks due to ligand field and exchange splitting.[2,17] The second peak, about 5–10 eV above threshold, is related to unoccupied O 2*p* states hybridized with metal 4*s* and 4*p* states.[2,17] The third region up to 30–50 eV above threshold relates to multiple scattering of the excited electron with low kinetic energy.[2] The O *K* prepeak is visible in the STO films. In the LMO and SMO regions, the O *K* prepeak has a significantly lower intensity than the first peak. The O *K* prepeak is also visible in the spectrum image of the O *K* edge shown in Fig. 4(a). The STO which has been lightly doped with Mn has a lower intensity O *K* prepeak.

Figure 5(b) is a closer look at the O *K* edge in the LMO films. Here, we show EELS spectra from the double layer LMO region and the single layer LMO region. The O prepeak is suppressed in the double layer of LMO, indicating a decrease of O 2*p* holes hybridized with Mn 3*d* in the double layer LMO. The O atoms in the MO layer are sandwiched between two LO layers in the case of the double layered LMO, whereas in the single layer of LMO, the same O atoms see LO and SO layers on two sides, which has a different electronic structure. The second peak in the O *K* edge of single layer and double layer LMO are shifted toward lower energy loss than the same peaks in SMO and STO. We also see that the second peak in the double layer LMO is shifted toward lower energy loss by ~1.5 eV. The decrease of the prepeak and shift of the second peak from SMO to LMO was observed by Verbeeck *et al.* in a 9×4 LMO-SMO superlattice, who suggested that these two trends are correlated.[15]

The Mn $L_{2,3}$ edge should allow one to determine the valence of the Mn.[10,19] The L_3 and L_2 peaks are due to transitions from 2*p* core states to unoccupied 3*d* states.[2,20] As the formal valence of Mn is increased, the L_3 peak tends to shift to higher energy.[2,10] The Mn $L_{2,3}$ edge in Fig. 4(a) shows essentially no peak shift within the detectable resolution between the LMO and SMO regions. This is surprising if we consider the nominal valences of Mn, which is 3+ in LMO and 4+ in SMO. The lack of peak shift was also observed by Verbeeck *et al.* in thicker LMO-SMO films. They argue that if changes in the O *K* edges state are seen, the Mn-O bonds have significant covalent character. However, Kurata *et al.* observed by EELS that the L_3 peak shifts to higher energy loss by 1–1.5 eV as the valence of the Mn ion is increased from 3+ to 4+ in bulk specimens.[2,21,22] Cramer *et al.* observed significant changes in peak shape as well as peak shifts of 1–2 eV in the *L*-edge structure in EXAFS spectra of bulk specimens with different Mn valence.[23] This peak shift should be visible in EELS if the Mn valence is changing since we detected peak shifts in the O *K* edge of 1–1.5 eV

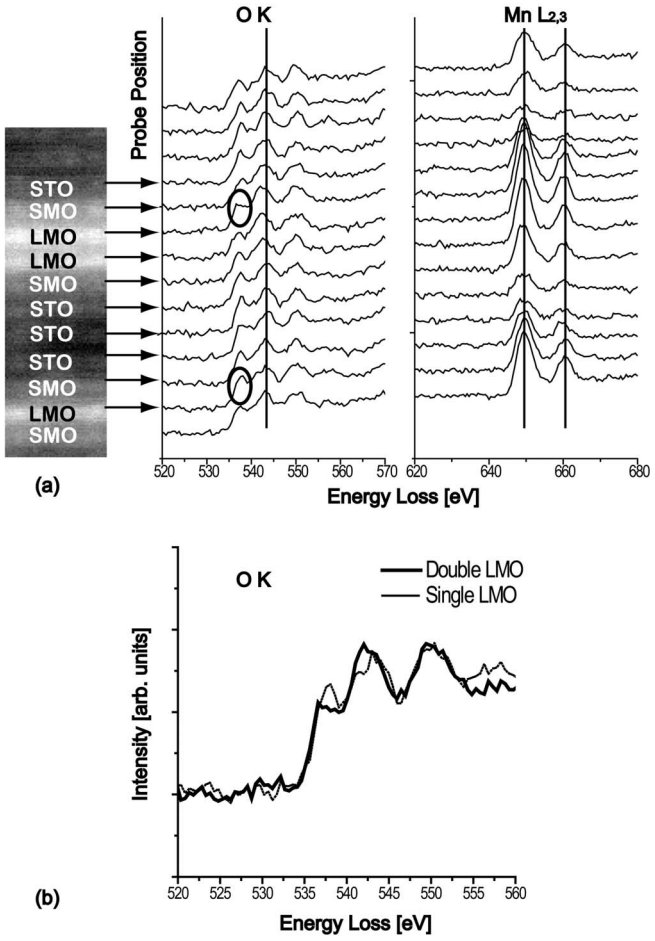

FIG. 5. (a) The energy-loss spectrum of the O *K* and Mn $L_{2,3}$ edges from the area indicated by the arrow in Fig. 4(a). The O prepeak indicated has a greater intensity in STO than SMO and LMO. The second O peak shifts in the thicker LMO films. In the Mn $L_{2,3}$ spectrum, there is no peak shift from SMO to LMO films within the detector resolution and energy spread. (b) The energy-loss spectrum of the O *K* edge in LMO films shows that the oxygen bonding in the single layer of LMO is strongly influenced by SMO and STO.

over single perovskite cell layers. The Mn ion valence appears constant across the SMO-LMO interfaces. The shift of the second O *K* peak indicates that the unoccupied states of O hybridized with metal 4*d* and 5*d* states are changing from LMO to SMO layers. One would expect a correlated change in Mn unoccupied 3*d* states. The depression of the prepeak of the O *K* edge in the double layered LMO indicates that the LMO should have different Mn 3*d* states than SMO. Since we do not observe a peak shift, our films may have similar character to the papers of Verbeeck *et al.*,[14,15] which suggest that the valence is not changing and that Mn in the LMO and SMO films are partially covalent.

The substrate and STO-SMO films are shown in Fig. 6. Ten unit cells of STO film are grown as a buffer layer on top of the substrate, and are assumed to have bulk properties. On top of this buffer layer are alternating SMO and STO films (see Fig. 1 for film growth). In this case, the probe size used for EELS acquisition was increased for higher signal to noise

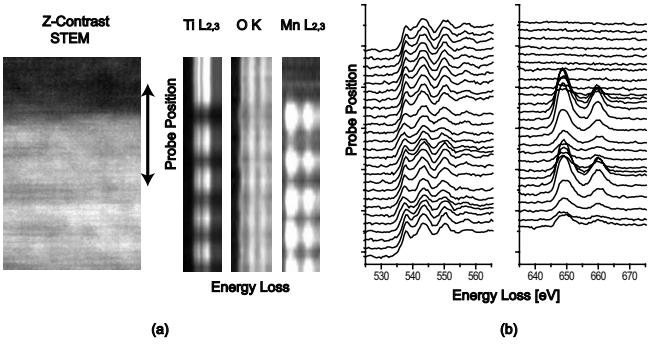

FIG. 6. STEM and EELS spectrum images of the superlattice at the substrate and STO-SMO films. The inserted spectra are the Ti $L_{2,3}$, O K, and Mn $L_{2,3}$. The O K preedge is visible in the STO layers. The O K preedge shifts in the different perovskite films. (b) The energy-loss spectrum of the O K and Mn $L_{2,3}$ edges from the area indicated by the arrow in (a). The O K peak is shifted slightly to the right in the SMO films compared to the substrate and STO films.

ratio. In the O K spectrum shown in Fig. 6(b), SMO films which are both three and four unit cells in thickness show a prepeak shift of ~1 eV in the center of the film. At the SMO-STO interfaces, the prepeak shifts less strongly. This indicates that the 1s core states of O are different in SMO films than bulk or thin film STO. We also observe that the second O peak is slightly rounder in SMO films and more triangular in STO films. This change is expected as the metal 4s and 4p states change when moving from Ti to Mn oxides.

In the Ti $L_{2,3}$ spectrum recorded from this region, we observe peak shifts at STO-SMO interfaces. Figure 7 shows the Ti $L_{2,3}$ spectra taken at the STO buffer layer (first curve), at the interface of 4 monolayers of SMO sandwiched between the STO buffer layer and four monolayers of STO film (bold curves), at the interface of three monolayers of SMO sandwiched between four monolayers of STO on both sides (dotted lines), and from a STO thin film (bottom curve). The substrate and thin film of STO show a similar Ti $L_{2,3}$ spectrum with no detectable peak shift and an L_3-L_2 splitting of ~5 eV. This splitting is similar to a 5.5 eV splitting measured by Leapman *et al.*[24] The Ti spectra at the interfaces with SMO show a peak shift of ~1 eV in the L_3 peak. A peak shift has also been observed by soft x-ray absorption spectroscopy and EELS in $LaTiO_3$-$SrTiO_3$ systems as the Ti valence changes from 4+ to 3+.[25,26] The valence of Mn in bulk SMO is 4+, as is the valence of Ti in bulk STO. However, in this case of Ti substituting for Mn, there is a peak

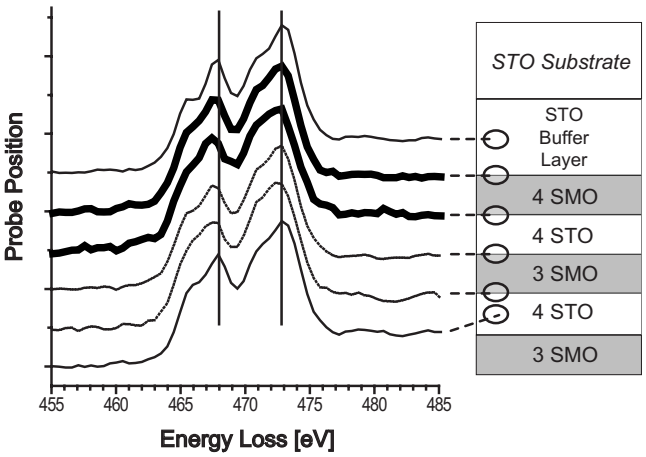

FIG. 7. The Ti $L_{2,3}$ peak position shifts at the STO-SMO interface and depends on the thickness of SMO.

shift in the Ti L_3 edge. Therefore, we believe that the peak shift in Ti $L_{2,3}$ at the STO-SMO interface would be even less if the SMO film was one or two layers thick. This would mean that the Ti valence at the interface can be controlled by changing the thickness of SMO.

In summary, we have grown a unique epitaxial superlattice structure and probed the physical structure with electron nanodiffraction and the electronic structure of interfaces with electron energy-loss spectroscopy. We have observed shifts in the O K edge of $LaMnO_3$ when the film thickness changes from one to two unit cells, and in the O K prepeak in $SrMnO_3$ and $SrTiO_3$ films. Within our instrument resolution, we do not observe peak shifts of Mn in $LaMnO_3$ and $SrMnO_3$, indicating that the valence of the Mn ion is constant across the interface. We also see that the titanium valence changes at the interface from $SrTiO_3$ to $SrMnO_3$.

ACKNOWLEDGMENTS

This material is based on work supported by the U.S. Department of Energy, Division of Materials Sciences under Grant No. DEFG02-91ER45439, through the Frederick Seitz Materials Research Laboratory at the University of Illinois at Urbana-Champaign. Research was carried out in the Center for Microanalysis of Materials, University of Illinois at Urbana-Champaign, which is partially supported by the U.S. Department of Energy under Grant No. DEFG02-91-ER45439.

[1] J. L. Maurice, D. Imhoff, J. P. Contour, and C. Colliex, Philos. Mag. **86**, 2127 (2006).
[2] H. Kurata and C. Colliex, Phys. Rev. B **48**, 2102 (1993).
[3] D. Fuks, S. Dorfman, J. Felsteiner, L. Bakaleinikov, A. Gordon, and E. A. Kotomin, Solid State Ionics **173**, 107 (2004).
[4] Y. Nohara, A. Yamasaki, S. Kobayashi, and T. Fujiwara, Phys. Rev. B **74**, 064417 (2006).
[5] Y. Tokura, Phys. Today **56** (7), 50 (2003).
[6] Y. Tokura and N. Nagaosa, Science **288**, 462 (2000).
[7] S. Okamoto and A. J. Millis, Nature (London) **248**, 630 (2004).
[8] A. Ohtomo, D. A. Muller, J. L. Grazul, and H. Y. Hwang, Nature (London) **219**, 378 (2002).
[9] T. Satoh, K. Miyano, Y. Ogimoto, H. Tamaru, and S. Ishihara, Phys. Rev. B **72**, 224403 (2005).

[10] L. Samet, D. Imhoff, J. L. Maurice, J. P. Contour, A. Gloter, T. Manoubi, A. Fert, and C. Colliex, Eur. Phys. J. B **24**, 179 (2003).
[11] H. Nakano, T. Mori, and N. Kamegashira, J. Alloys Compd. **242**, 179 (2002).
[12] O. I. Lebedev, J. Verbeeck, G. Van Tendeloo, C. Dubourdieu, M. Rosina, and P. Chaudouet, J. Appl. Phys. **94**, 7646 (2003).
[13] T. Koida, M. Lippmaa, T. Fukumura, K. Itaka, Y. Matsumoto, M. Kawasaki, and H. Koinuma, Phys. Rev. B **66**, 144418 (2002).
[14] J. Verbeeck, O. I. Lebedev, G. Van Tendeloo, J. Silcox, B. Mercey, M. Hervieu, and A. M. Haghiri-Gosnet, Appl. Phys. Lett. **79**, 2037 (2001).
[15] J. Verbeeck, O. I. Lebedev, G. Van Tendeloo, and B. Mercey, Phys. Rev. B **66**, 184426 (2002).
[16] M. Abbate, F. M. F. de Groot, J. C. Fuggle, A. Fujimori, O. Strebel, F. Lopez, M. Domke, G. Kaindl, G. A. Sawatzky, M. Takano, Y. Takeda, H. Eisaki, and S. Uchida, Phys. Rev. B **46**, 4511 (1992).
[17] F. M. F. de Groot, M. Grioni, J. C. Fuggle, J. Ghijsen, G. A. Sawatzky, and H. Petersen, Phys. Rev. B **40**, 5715 (1989).
[18] L. A. Grunes, R. D. Leapman, C. N. Wilker, R. Hoffmann, and A. B. Kunz, Phys. Rev. B **25**, 7157 (1982).
[19] F. Pailloux, D. Imhoff, T. Sikora, A. Barthelemy, J. L. Maurice, J. P. Contour, C. Colliex, and A. Fert, Phys. Rev. B **66**, 014417 (2002).
[20] C. W. M. Castleton and M. Altarelli, Phys. Rev. B **62**, 1033 (2000).
[21] J. H. Rask, B. A. Miner, and P. R. Buseck, Ultramicroscopy **21**, 321 (1987).
[22] J. H. Paterson and O. Krivanek, Ultramicroscopy **32**, 319 (1990).
[23] S. P. Cramer, F. M. F. de Groot, Y. Ma, C. T. Chen, F. Sette, C. A. Kipke, D. M. Eichhorn, M. K. Chan, W. H. Armstrong, E. Libby, G. Christou, S. Brooker, V. McKee, O. C. Mullins, and J. C. Fuggle, J. Am. Chem. Soc. **113**, 7937 (1991).
[24] R. D. Leapman, L. A. Grunes, and P. L. Fejes, Phys. Rev. B **26**, 614 (1982).
[25] M. Abbate, F. M. F. de Groot, J. C. Fuggle, A. Fujimori, Y. Tokura, Y. Fujishima, O. Strebel, M. Domke, G. Kaindl, J. van Elp, B. T. Thole, G. A. Sawatzky, M. Sacchi, and N. Tsuda, Phys. Rev. B **44**, 5419 (1991).
[26] A. Ohtomo, D. A. Muller, J. L. Grazul, and H. Y. Hwang, Appl. Phys. Lett. **80**, 3922 (2002).